

Transients Obscured by Dusty Disks

C. S. Kochanek^{1,2}

¹ *Department of Astronomy, The Ohio State University, 140 West 18th Avenue, Columbus OH 43210*

² *Center for Cosmology and AstroParticle Physics, The Ohio State University, 191 W. Woodruff Avenue, Columbus OH 43210*

23 May 2023

ABSTRACT

Dust absorption is invoked in a number of contexts for hiding a star that has survived some sort of transient event from view. Dust formed in a transient is expanding away from the star and, in spherical models, the mass and energy budgets implied by a high optical depth at late times make such models untenable. Concentrating the dust in a disk or torus can in principle hide a source from an equatorial observer using less mass and so delay this problem. However, using axisymmetric dust radiation transfer models with a range of equatorial dust concentrations, we find that this is quite difficult to achieve in practice. The polar optical depth must be either low or high to avoid scattering optical photons to equatorial observers. Most of the emission remains at wavelengths easily observed by JWST, and the equatorial brightness is reduced by at most a factor of ~ 2 compared to isotropic emission even for equatorial (visual) optical depths of 10^3 . It is particularly difficult to hide a source with silicate dusts because the absorption feature near $10\mu\text{m}$ frequently leads to the emission being concentrated just bluewards of the feature, near $8\mu\text{m}$.

Key words: stars: massive – supernovae: general – supernovae

1 INTRODUCTION

There are several classes of transients in which dust forms and obscures the surviving progenitor or is argued to form in order to explain the apparent absence of a surviving progenitor at optical or near-IR wavelengths. In the first category are eruptions such as η Car (e.g., Humphreys & Davidson 1994) and stellar mergers such as V838 Mon (e.g., Bond et al. 2003). In the second category are debated transients such as the supernova impostors like SN 1997bs (e.g., Van Dyk et al. 2000, Adams & Kochanek 2015) and SN 2008S (e.g., Prieto et al. 2008, Thompson et al. 2009, Kochanek 2011, Adams et al. 2016) or the proposed failed supernovae NGC 6946-BH1 (Gerke, Kochanek, & Stanek 2015, Adams et al. 2017, Basinger et al. 2021).

With the constraining powers of ground based observatories, Hubble (HST) and Spitzer (SST) Space Telescopes it is feasible to hide stars with the luminosities of these progenitor systems from detection in nearby galaxies ($\lesssim 10$ Mpc) with spherical shells of dusty ejecta. The optical depth and ejecta radius must simply be made large enough to push the escaping emission to long enough wavelengths to evade detection: sufficiently absorbed in the optical and near-IR to be invisible or lost amid the overlapping sea of red giants, and with dust emission cold enough to slip under the sensitivity limits of (generally) warm SST at 3.6 and $4.5\mu\text{m}$. Hiding the emission will become much more challenging in

the era of JWST since it can easily detect such sources out to $\sim 25\mu\text{m}$ with vastly better angular resolution for avoiding confusion with either other stars or diffuse emission.

The combination of near-IR and bluer mid-IR observations generally rule out sources obscured by dust forming in an on-going wind. Dust rapidly forms once temperatures drop below the condensation temperature so, combined with the expansion, the optical depth of a dusty wind is concentrated near its base. Thus, a high optical depth wind immediately converts the emission from the central source into hot ($T_d \sim 1000$ K) dust emission. It then takes extremely high optical depths to absorb these photons further out in the wind and shift the peak of the escaping emission beyond $5\mu\text{m}$.

Colder dust emission is most easily achieved by forming dust in material ejected in the transient. Dust forms and is initially hot, but then becomes cooler as the ejecta moves outwards. Dust growth ceases shortly after it forms, because the collisional growth rates are dropping as $r^{-2} \propto t^{-2}$ due to the expansion. The dust opacity is then constant, and the mean optical depth must drop as t^{-2} assuming a constant expansion velocity and mass conservation. The effective optical depth could drop more rapidly than t^{-2} if the expanding shell starts to fragment due to instabilities, leading to the radiation escaping through lower optical depth channels in the ejecta.

The observed spectral energy distribution (SED) of the

source can be used to constrain the luminosity (L_*) and temperature (T_*) of the central source, the temperature of the dust (T_d) and the visual optical depth τ of the shell.¹ The detailed structure of the SED depends on the composition of the dust through the wavelength-dependent opacities, and inferences about the mass of the ejecta depend on the dust-to-gas mass ratio. To order of magnitude, the grain temperature is set by the available flux, $\sigma T_d^4 = L_*/16\pi r^2$, so constraints on the overall luminosity and the dust temperature provides an estimate of the dust radius r which leads to an estimate of the expansion velocity v_e assuming $r = v_e \Delta t$ after elapsed time Δt . Given an estimate of the visual opacity κ , the SED model also provides an estimate of the ejecta mass and kinetic energy. For a thin shell $\tau = M_e \kappa / 4\pi r^2$, so

$$M_e = \frac{4\pi r^2 \tau}{\kappa} = \frac{L_* \tau}{4\kappa \sigma T_d^4} \quad (1)$$

and

$$E_e = \frac{2\pi r^4 \tau}{\Delta t^2 \kappa} = \frac{L_*^2 \tau}{128 \Delta t^2 \kappa \sigma^2 T_d^8}. \quad (2)$$

For the debated systems with non-detections, the question then becomes whether the velocities, masses and energies required to make the dust cold enough to avoid detection are plausible. Time will also tell, since in any model dependent on an expanding shell, the shell eventually becomes transparent.

Where quantitative models are made for the SEDs of these sources, they use spherically symmetric models, principally based on the dust radiation transfer code `DUSTY` (Ivezic & Elitzur 1997, Ivezic, Nenkova, & Elitzur 1999). Such models have two shortcomings. First, there is no reason the ejecta needs to be spherically symmetric. In particular, there are invocations of models with more equatorial than polar material with the observer near the equatorial plane as a means of evading the limits implied by the spherical SED models (e.g., Kashi & Soker 2017, Andrews et al. 2021, Bear, Soker, & Kashi 2022). Second, there is no reason that the density distribution should remain homogeneous. Expanding shells tend to develop instabilities, instabilities lead to clumping of the material, and this produces lower optical depth channels through which radiation can escape. If instabilities develop, the effective optical depth will drop faster than the $\tau \propto t^{-2}$ drop of the mean optical depth.

In this paper we explore the first question, the effect of deviations from spherical symmetry, by examining the SEDs produced by axisymmetric dusty shells with large differences between the equatorial and polar optical depths. For the optical and near-IR light, the primary effect is that the polar dust can scatter emission that would be absorbed if trying to directly escape along the equator into the line of sight of an equatorial observer. In the mid-IR, a polar observer sees both less obscured direct emission from the central source and dust emission with a broad range of temperatures from the highly obscured regions. Naively, the equatorial observer

¹ Optical depths in the text are all visual band (0.55 μ m) effective optical depths $\tau = (\tau_a(\tau_s + \tau_a))^{1/2}$ given the absorption and scattering optical depths τ_a and τ_s . The effective optical depth takes into account the extra path length created by the scattering. For the disk models, the polar and equatorial visual effective optical depths are τ_p and τ_e .

sees reduced and colder emission. We describe the model used in §2, present the results in §3 and discuss their consequences in §4.

2 MODEL

We used the `RADMC-3D` (Dullemond et al. 2012) Monte Carlo dust radiation transfer package to carry out the calculations in axisymmetry with reflection symmetry about the equator. We used the disk dust density model from Ueta & Meixner (2003),

$$\rho_d = \frac{[\tau_p + (\tau_e - \tau_p)(1 - |\cos \theta|)^\eta]}{R_{in} \kappa} \left(1 - \frac{R_{in}}{R_{out}}\right)^{-1} \left(\frac{R_{in}}{R}\right)^2$$

where τ_p and τ_e are the optical depths at the pole and the equator ($\tau_e > \tau_p$), R_{in} and R_{out} are the inner and outer edges of the dust shell, and η controls the concentration of the dust towards the equatorial plane, as illustrated in Fig. 1. Larger values of η more strongly concentrate the dust towards the equator. We normalize the optical depths at V-band (0.55 μ m) based on the effective absorption opacity $\kappa = (\kappa_a(\kappa_a + \kappa_s))^{1/2}$ given the absorption κ_a and scattering κ_s opacities. The effective absorption takes into account the increase in absorption due to scattering lengthening the distance a photon travels. The mass of the shell is

$$M_{ej} = \frac{4\pi R_{in} R_{out} \tau_e}{f_d \kappa} \frac{1 + \eta \tau_p / \tau_e}{1 + \eta} \quad (3)$$

where $f_d \simeq 0.005$ is the dust mass fraction in the shell. If $\tau_p / \tau_e \ll 1$, then the shell mass is $(1 + \eta)^{-1}$ less than a spherical shell with the equatorial optical depth τ_e – the dust has to be very equatorially concentrated (large η) before there is a large change in the required mass. If the expansion velocity is v_e and the elapsed time is Δt so that $R_{in} = v_e \Delta t$, the ejecta mass is

$$M_e = 6.3 \frac{\tau}{100} \frac{R_{out}}{R_{in}} \left(\frac{v_e}{10^3 \text{ km/s}} \frac{\Delta t}{10 \text{ yr}}\right)^2 \left(\frac{100 \text{ cm}^2/\text{g}}{f_d \kappa}\right) \times \frac{1 + \eta \tau_p / \tau_e}{1 + \eta} M_\odot \quad (4)$$

and the kinetic energy, assuming everything has a velocity of v_e , is

$$K_e = 0.062 \frac{\tau}{100} \frac{R_{out}}{R_{in}} \left(\frac{v_e}{10^3 \text{ km/s}}\right)^4 \left(\frac{\Delta t}{10 \text{ yr}}\right)^2 \left(\frac{100 \text{ cm}^2/\text{g}}{f_d \kappa}\right) \times \frac{1 + \eta \tau_p / \tau_e}{1 + \eta} \text{ FOE} \quad (5)$$

where 1 FOE = 10⁵¹ erg is the characteristic energy of a supernova. Assuming the velocity is the same for all material is equivalent to assuming the shell thickness is due to the duration of the event rather than a spread in velocity. If we instead linearly increase the velocity with shell radius to explain the thickness, the kinetic energy would increase by $(R_{in}^2 + R_{in} R_{out} + R_{out}^2) / 3R_{in}^2$ or a factor of 7/3 for $R_{out} = 2R_{in}$.

We used a log normal grain size distribution with a mean radius of 0.1 μ m and a width of 0.05 μ m (i.e., 0.3 dex). We generated the opacity tables with `OpTool` (Dominik, Min, & Tazaki 2021) and their default Distribution of Hollow Spheres (DHS, Min, Hovenier, & de Koter 2005) opacity model. We used the pyroxene silicate dust

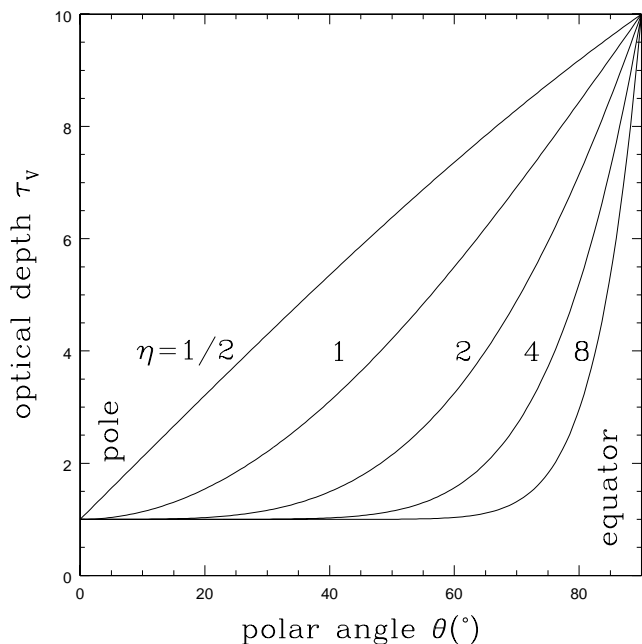


Figure 1. Examples of the polar angle dependent optical depth produced by Eqn. 2 with an equatorial optical depth of $\tau_e = 10$, a polar optical depth of $\tau_p = 1$ and exponents of $\eta = 1/2, 1, 2, 4$ and 8.

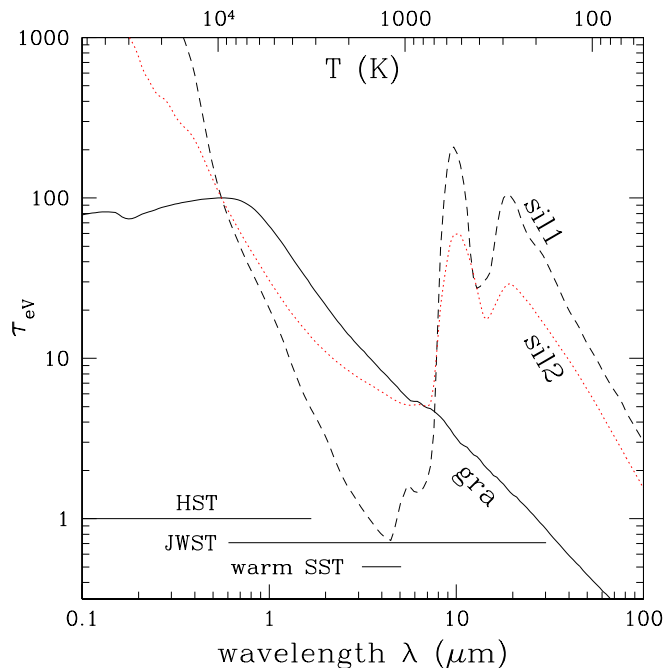


Figure 2. The wavelength dependence of the effective optical depth for the graphitic gra (black solid) and silicate sil1 (black dashed) and sil2 (red dotted) dust models normalized to have an effective visual ($0.55\mu\text{m}$) optical depth of $\tau = 100$. The upper axis gives the temperature corresponding to the mean photon energy ($T = hc/2.7k\lambda$). Horizontal bars at bottom show the wavelength ranges spanned by HST, warm SST and JWST.

model (model “sil1”, Dorschner et al. 1995) and the Draine (2003) graphitic (model “gra”) and astrosilicate (model “sil2”) dust models. Fig. 2 shows the wavelength dependence of the effective absorption optical depth for the three models normalized to a visual optical depth of $\tau = 100$. One important difference between them for the results is that graphitic dusts lack the strong silicate absorption feature at $10\text{--}20\mu\text{m}$. One reason for including the two silicate models is to explore the role of this feature, where the sil1 model has a peak mid-IR opacity greater than its V band opacity, while the sil2 model has a weaker peak. The other important difference is that the silicate dusts have much higher scattering opacities. At $0.55\mu\text{m}$, the absorption, scattering and effective opacities are $(\kappa_a, \kappa_s, \kappa) = (380, 8700, 1900)$, $(2600, 9300, 5600)$, and $(93000, 39000, 110000)$ cm^2/g for the sil1, sil2 and gra models, respectively. Scattering is important only for the UV and optical – it becomes steadily less important relative to absorption moving into the infrared. Fig. 2 also shows the wavelength ranges covered by HST (WFC3/IR not NICMOS), warm SST and JWST to illustrate the wavelength ranges where observations are feasible.

For these experiments, we model the central source based on the progenitor of NGC 6946-BH1. The central star is a black body treated as a point source with luminosity $L_* = 3 \times 10^5 L_\odot$ and temperature $T_* = 4000$ K. We include dust scattering, but RADMC-3D is restricted to isotropic scattering for calculations in two dimensions unless doing a full scattering analysis with polarization. We used the simpler, faster mode with isotropic scattering. We used 100 radial zones between R_{min} and $R_{max} = 2R_{min}$ and 90 angular zones between the equator and the pole. The dust temperature was set using 10^6 photon packets, ten times the RADMC-3D default and the SEDs were generated using its default parameters.

We used an expansion velocity of $v_e = 10^3$ km/s and considered expansion times of $\Delta t = 1, 3, 5,$ and 10 years, leading to $R_{in} = 632, 1054, 2108,$ and 4216 AU ($10^{15.98}, 10^{16.20}, 10^{16.50}$ and $10^{16.80}$ cm). Only the radius is actually relevant, and these could just as well represent a system with $v_e = 200$ km/s expanding for 15, 25, 50 and 100 years. Similarly, changes in distance or time can also be viewed as changes in luminosity since the emission is really controlled by L_*/r^2 . We ran models with polar optical depths of $\tau_p = 0.1, 1.0$ and 3.0 and equatorial optical depths of $\tau_e = 10, 30, 100, 300$ and 1000 over the range equatorial concentration power law indices from $\eta = 0.5$ to 8.0 (see Fig. 1). For comparison, we also ran spherically symmetric models at each optical depth.

3 RESULTS

Figs. 3 through 7 survey the results as functions of η and τ_e for fixed $\tau_p = 1$ and $\Delta t = 3$ yr. The results are shown for $\tau_e = 10, 30, 100$ and 300 and all three dust types with one figure for each of $\eta = 1/2, 1, 2, 4$ and 8 , corresponding to an increasingly disk-like dust distribution (see Fig. 1). The emergent spectral energy distribution (SED) is shown for viewing angles from pole-on (0°) to edge on (90°) in increments of 10° , along with the SEDs for spherical models with the two limiting optical depths of τ_e and τ_p .

If we focus first on the graphitic models with $\eta = 1$ in

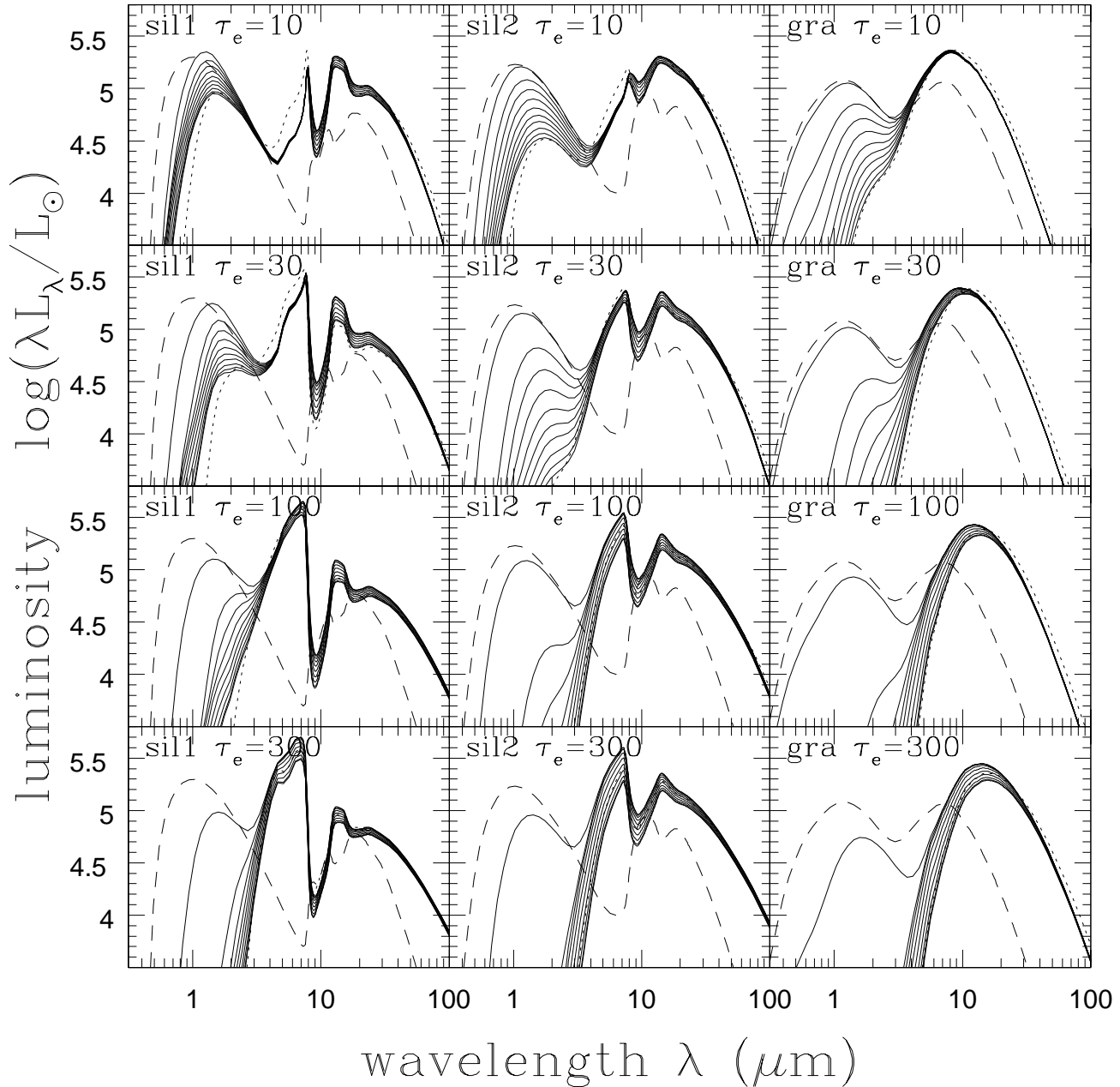


Figure 3. Spectral energy distributions for models with $\eta = 1/2$, $\Delta t = 3$ yr, polar optical depth $\tau_p = 1$ and equatorial optical depths of $\tau_e = 10$ (top), 30 (middle), 100 (middle) and 300 (bottom) for the sil1 (left), sil2 (middle) and graphitic (right) dusts. The solid lines are the SEDs of the disk models viewed from 0° (pole-on, most optical emission) to 90° (edge on, least optical emission) in increments of 10° . The dashed (dotted) line is the SED for a spherical model with an optical depth of τ_p (τ_e).

Fig. 4 we see that the optical and near-IR emission smoothly shifts between the two limiting spherical models with viewing angle. As the equatorial optical depth increases, the star steadily becomes optically “invisible” to higher and higher latitudes. The mid-IR emission lies between the two limiting cases but fairly close to the τ_e spherical model - for example, the spherical models absorb 63% ($\tau = 1$) and 100% ($\tau = 10$) of the optical emission, respectively, while the disk model with $\tau_e = 10$ absorbs 99% and so the total mid-IR emission is very close to the higher optical depth

spherical model, although the dust emission is slightly hotter. As we raise τ_e , the optical depth of the disk starts to become important at the wavelengths of the dust emission. The longer wavelengths continue to simply escape but the shorter wavelengths begin to preferentially escape along directions away from the disk. Nonetheless, the mid-IR emission peak is bluer than the high optical depth spherical model from all viewing directions.

Two issues make the behavior of the silicate models quite different. The first is that the silicate dust has a much

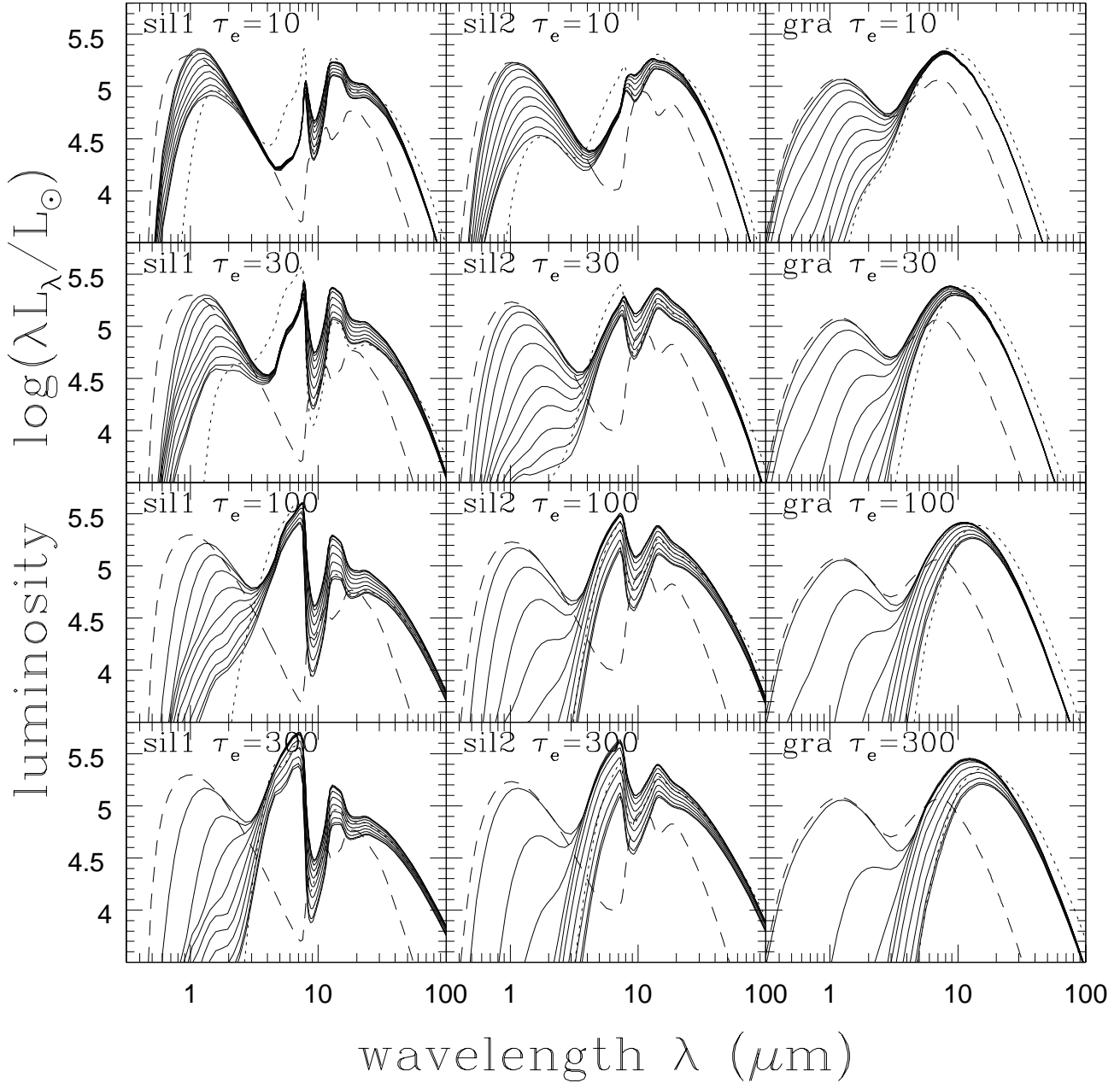


Figure 4. Same as Fig. 3 but for $\eta = 1$.

higher scattering opacity in the optical. Thus, if we look at the optical SEDs for the silicate models, we always see significantly more optical emission than in the high optical depth spherical model even when viewed from the equator. Optical photons heading towards the polar regions are scattered to observers closer to the equator through the reduced optical depth regions higher above the equatorial plane. This means, however, that the polar optical emission is less than in the low optical depth spherical model. The photons scattered to the equatorial observers are not replaced by initially equatorially directed photons being scattered towards the poles because they are absorbed in the disk.

The second difference comes from the strong mid-IR absorption features discussed earlier (Fig. 2). In the low optical depth spherical models, the effects of the absorption features are modest. However, in the high optical depth models, the structure of the SED is the inverse of the opacity, with emission peaking on the blue side of the absorption feature, a strong dip in emission at the opacity peak near $10\mu\text{m}$, a weaker emission peak at the dip in the opacity near $20\mu\text{m}$ and then a smoother decline at longer wavelengths. As the equatorial optical depth increases, the emission on the blue side of the mid-IR opacity peak strengthens while the emission on the red side remains similar to the spherical model.

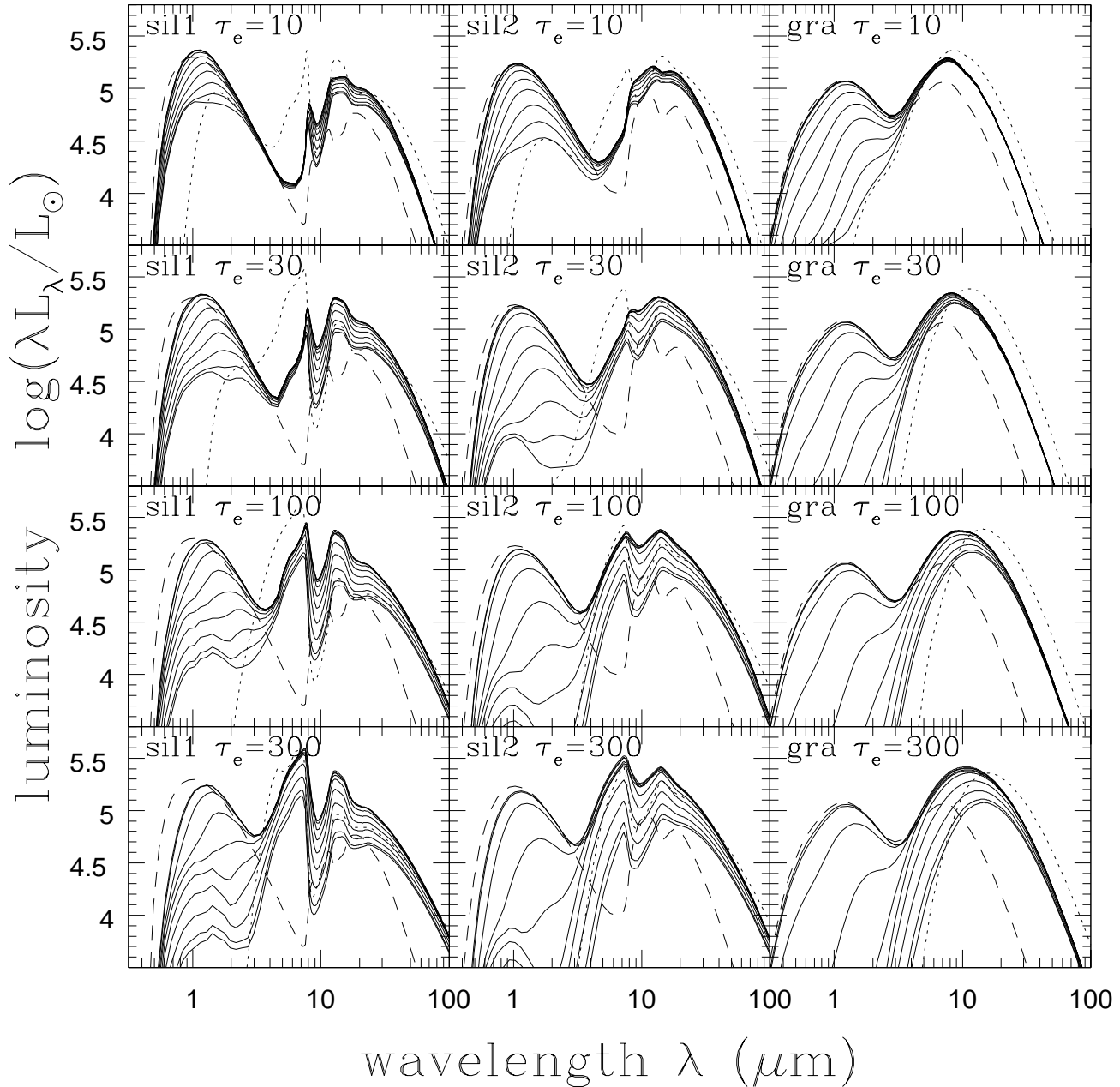


Figure 5. Same as Fig. 3 but for $\eta = 2$.

We can understand this as a version of the greenhouse effect created by the structure of the silicate opacity in Fig. 2. The opacity has a tremendous drop on the blue side of the peak near $10\mu\text{m}$, but only a slow tail-off on the red side. So if the dust has a temperature corresponding to wavelengths around the opacity peak, and the optical depth is high, then photons bluer than $10\mu\text{m}$ escape relatively easily while redder photons are reabsorbed. To reach a radiative equilibrium, the dust heats up until it can radiate enough energy in the opacity trough to balance the heating. As the optical depth increases, the absorption of redder photons increases faster than that of the bluer pho-

tons, so the emission in the opacity trough increases relative to the longer wavelength emission. The emission at $\sim 8\mu\text{m}$ becomes steadily stronger as the equatorial opacity increases even when viewed from the equator.

For the less diskier $\eta = 1/2$ models in Figs. 3, the SEDs simply shift to more closely resemble the high optical depth spherical models. The polar optical emission is reduced, as is the scattered light contribution to more equatorial observers. The silicate emission peak also becomes stronger and more closely resembles the spherical models.

As we now consider the diskier models in Figs. 5 through 7 there are two primary changes. First, it becomes easier

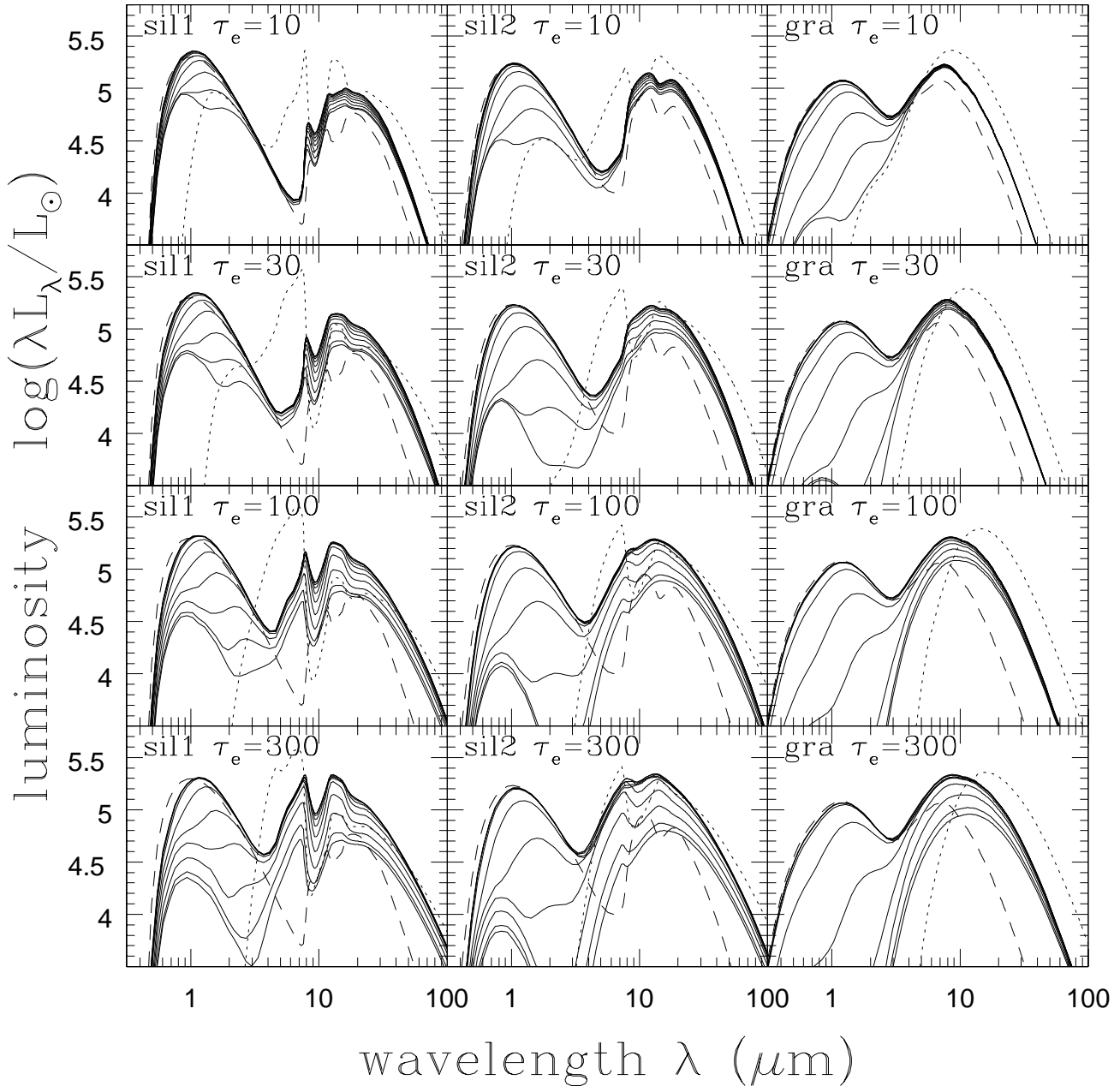


Figure 6. Same as Fig. 3 but for $\eta = 4$.

to scatter optical photons to an equatorial observer. Once a photon emitted upwards is scattered, a thinner disk has less optical depth for reabsorbing it when it is scattered towards an equatorial observer. For the same equatorial optical depth, there is also simply more escaping optical light because the concentration of the dust towards the equator means there is less absorption at intermediate latitudes. For example, averaging $\exp(-\tau)$ over inclination for $\tau_p = 1$ and $\tau_e = 100$, the fraction of V band photons escaping is 7.5×10^{-5} , 0.004, 0.033, 0.11 and 0.20 for $\eta = 1/2, 1, 2, 4$ and 8, respectively.

Second, the optical depth difference between moving

out through the disk versus perpendicular to the disk becomes increasingly large. For our angular structure in the limit that $\tau_p \rightarrow 0$ and we extend the dust distribution to $R_{out} \rightarrow \infty$, the ratio of the optical depth from the equator perpendicular to the disk or radially through the disk is 0.83 for $\eta = 1/2$ and drops to 0.57, 0.35, 0.21 and 0.11 for $\eta = 1, 2, 4$ and 8, respectively. This will lead to more of the mid-IR emission escaping towards the poles compared to the $\eta = 1/2$ model. For the graphitic dust, this makes the SED shift bluewards away from the high optical depth spherical model and closer to the lower optical depth spherical model. For the silicate dusts, the strength of the features created by

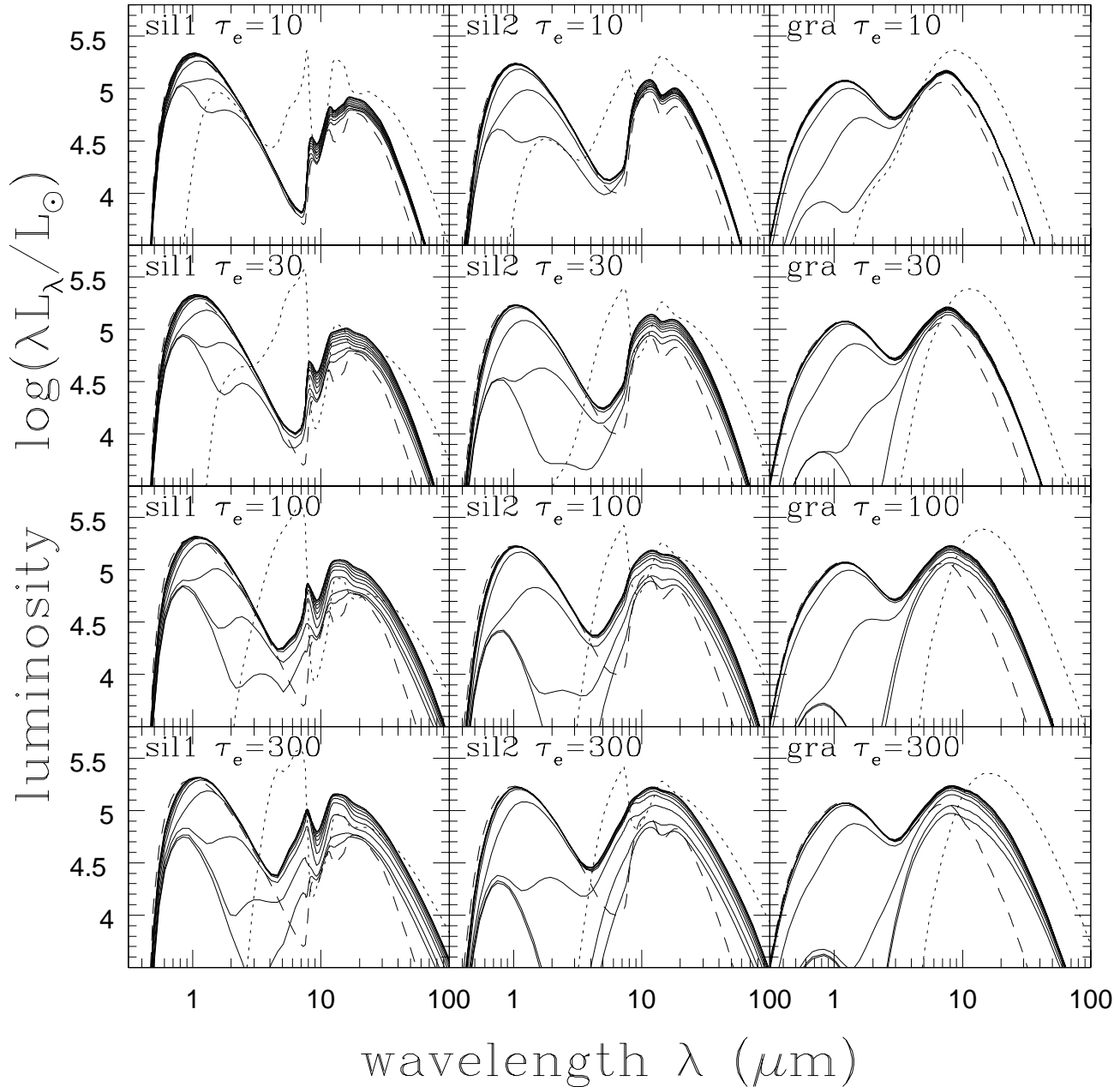


Figure 7. Same as Fig. 3 but for $\eta = 8$.

the silicate opacity bump weakens and the SEDs resemble those of a more disk (higher η) and lower equatorial optical depth model.

Fig. 8 shows the inferred isotropic luminosities for the $\eta = 1/2$ (Fig. 3), $\eta = 2$ (Fig. 5) and $\eta = 8$ (Fig. 7) as a function of viewing angle and equatorial optical depths of $\tau_e = 10, 30, 100, 300$ and 1000 with $\tau_p = 1$ and $\Delta t = 3$ years. By isotropic luminosity we mean integrating over the observed SED and assuming the source would have the same SED if viewed from any direction, and we compare it to the true luminosity L_* . As can roughly be inferred from the SEDs, the isotropic luminosity is generally fairly similar to

the true luminosity. Viewed pole-on, the isotropic luminosity is higher because the observer receives both significant optical emission and infrared emission from the disk. Viewed edge-on, the isotropic luminosity is lower because there is little or no optical emission and the infrared emission is modestly reduced. But even for the very disk ($\eta = 8$) models with very high optical depths ($\tau_e = 1000$), the isotropic luminosities are only off from the true luminosities by factors of ~ 2 . The variation with inclination then declines for less disk configurations (lower η) or lower equatorial optical depths. This gibes with the illuminated slab models considered in Adams et al. (2017), which found that even with no

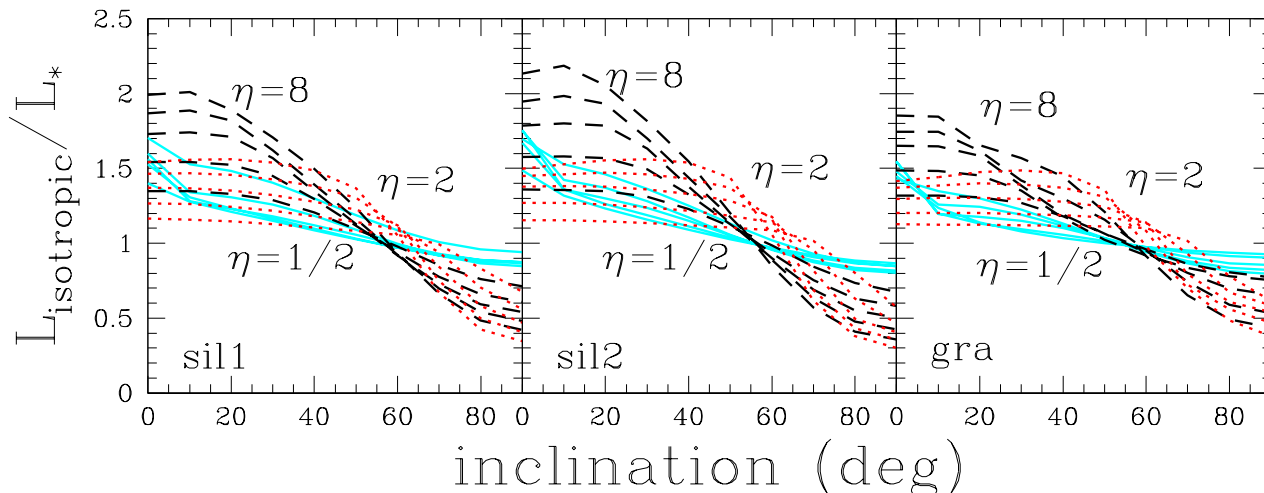


Figure 8. The isotropic luminosity $L_{isotropic}$ inferred from the SEDs in Figs. 3-7 as a function of viewing inclination angle (0° is pole-on, 90° is edge-on) relative to the true luminosity L_* for the sil1 (left), sil2 (middle) and gra (right) dusts. Results are shown for $\eta = 1/2$ (cyan solid), $\eta = 2$ (black dashed) and $\eta = 8$ (red dotted) and optical depths of $\tau_e = 10$ (least dependence on inclination), 30, 100, 300 and 1000 (strongest dependence on inclination) for fixed $\tau_p = 1$. Even for a $\tau_e = 1000$ disk viewed exactly edge on, the isotropic luminosity is within a factor of ~ 2 of the true luminosity.

emission able to escape to the observer through lower optical depth, higher latitude regions above the disk, the isotropic luminosity was only reduced by a factor of ~ 4 .

Fig. 9 shows the consequences of changing the polar extinction over the range $\tau_p = 0.1, 0.3, 1.0$ and 3.0 for $\tau_e = 100$, $\eta = 8$ and $\Delta t = 3$ years. The optical emission of the graphitic model is simply increasingly suppressed. Because of the greater importance of scattering for the silicate the equatorial optical emission initially increases with τ_p even as the polar emission decreases. The increasing polar optical depth also drives a strengthening of the mid-IR silicate emission feature, similar to the effects from reducing η . Only when the polar optical depth becomes sufficiently high does the optical equatorial emission begin to drop again.

Finally, in Fig. 10 we show how the SEDs of the $\eta = 8$ models with $\tau_e = 100$ and $\tau_p = 1$ depend on the dust radius, phrased as observation times of $\Delta t = 1, 3, 5$ and 10 years assuming an expansion velocity of $v_e = 10^3$ km/s. This is not a true time sequence because we are holding the optical depths fixed. If we started the sequence with $\tau_e = 100$ at $\Delta t = 1$ year, the optical depths would be $\tau_e = 11, 4$ and 1 at the later times. To actually have $\tau_e = 100$ at $\Delta t = 10$ years, the optical depth at $\Delta t = 1$ year would have to be $\tau_e = 10^4$!

Not surprisingly, the optical and near-IR emission depends little on the radius to the dust. The geometry of absorbing and scattering these photons is essentially self-similar. The mid-IR emission changes because the flux heating the dust is dropping. The SED peak shifts to longer wavelengths, roughly like the black body prediction of $\lambda \propto \Delta t^{1/2}$, and the silicate emission peak weakens. The development of the deep minimum in the SED at $5\text{-}10\mu\text{m}$ would make it relatively easy for these models to evade detection by warm SST. This is particularly true for the silicate models, where the high optical depth spherical models all produce an emission peak at these wavelengths. The mid-IR emission peak still lies at wavelengths easily probed by JWST.

4 DISCUSSION

Disky dust distributions have been invoked in a number of contexts to try to better hide stars posited to have survived an eruptive transient from detection (e.g., Kashi & Soker 2017, Andrews et al. 2021, Bear, Soker, & Kashi 2022). They have the advantage that they require less mass and energy to maintain a significant optical depth towards an equatorial observer at late times than a spherical distribution of the same optical depth. It was also generally assumed that a large fraction of the dust emission which would have been sent towards an equatorial observer in a spherical geometry would instead escape towards the poles, making the source significantly dimmer in the mid-IR.

Unless the dust distribution is carefully arranged, using a disk geometry will tend to enhance the optical emission seen by an equatorial observer. Photons scatter off dust above the disk and then can propagate to an equatorial observer. This can be minimized by having no modest optical depth paths from the source to the observer – either no polar dust, or enough polar dust that optical emission perpendicular to the disk is also heavily absorbed. This is especially true for silicate dusts with their higher optical scattering opacities.

For silicate dusts, a disk geometry can significantly reduce the emission at $5\text{-}10\mu\text{m}$ compared to spherical models. This is a consequence of the strong $10\mu\text{m}$ silicate dust absorption feature, which drives a significant emission peak on the blue side of the absorption in the spherical models. The feature still exists for the diskier models, but it can be considerably weaker and becomes weaker for diskier geometries and colder dust. The changes in the mid-IR emission for graphitic dust are much smaller because the opacity simply declines monotonically to longer wavelengths. The mid-IR emission beyond $10\mu\text{m}$ is shifted to bluer wavelengths than a spherical model with the same optical depth as the disk.

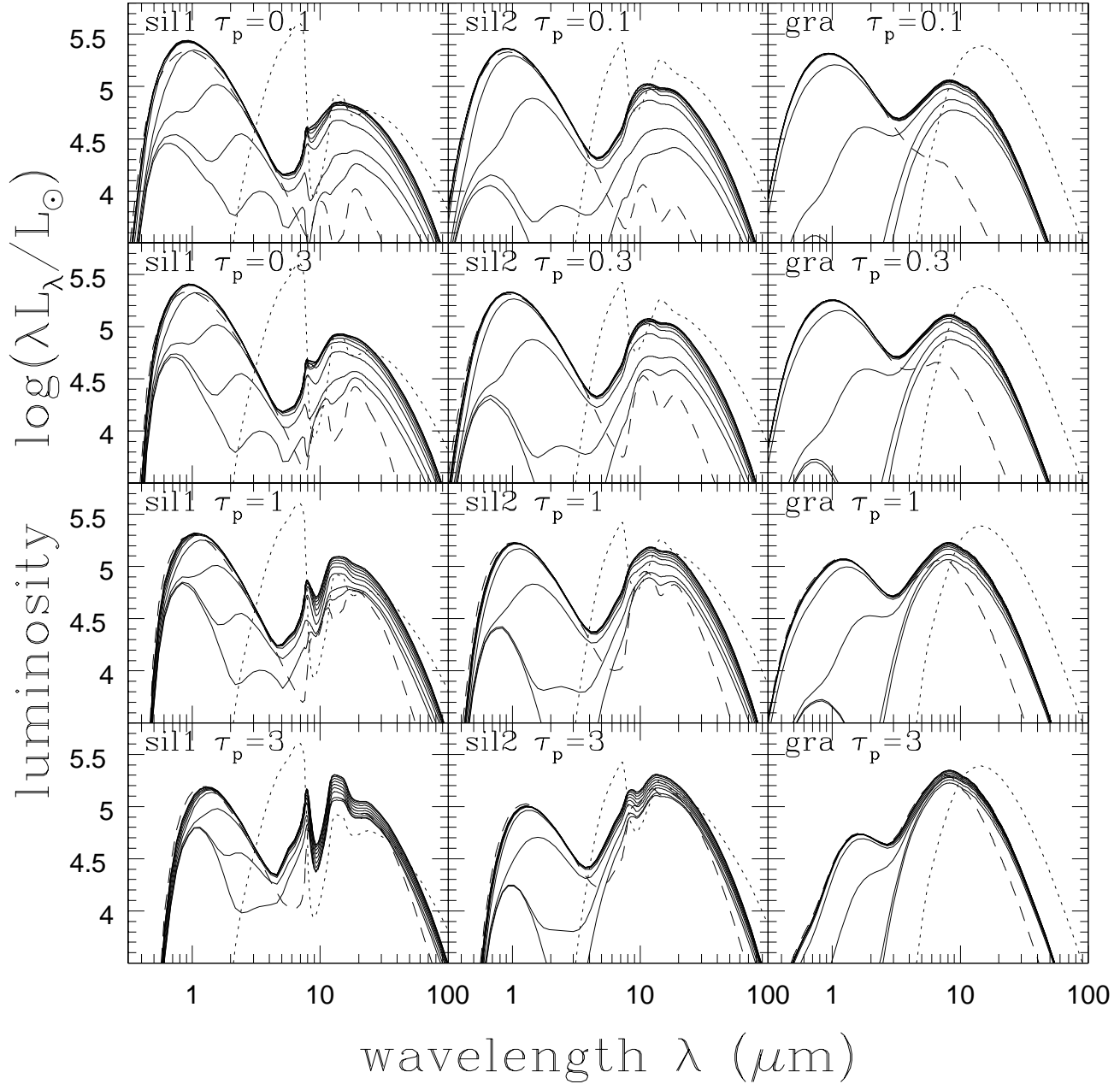


Figure 9. The effect of varying the polar optical depth over the range $\tau_p = 0.1$ (top), 0.3, 1.0 and 3.0 (bottom) with $\tau_e = 100$, $\eta = 8$ and $\Delta t = 3$ years for the sil1 (left), sil2 (middle) and gra (right) dusts. The SEDs are again shown for inclinations of 0° (pole-on) to 90° (edge-on) in increments of 10° and the dotted and dashed lines are for spherical models with optical depths of τ_e and τ_p , respectively.

None of the models strongly suppress the equatorial flux compared to a spherical model. The isotropic luminosities of the disk models are only suppressed in the equatorial direction by a factor of ~ 2 even when the optical depth through the disk is $\tau_e = 10^3$. Similarly, the polar isotropic luminosities are only enhanced by similarly modest factors. Adams et al. (2017) had already noted that even an infinite slab of dust with similar optical depths was only reducing the isotropic luminosity by a factor of 4 despite having no low optical depth paths between the observer and the source.

It was always possible to hide stellar luminosity sources at optical, near-IR and warm-SST mid-IR, which could only characterize the emission bluewards of $5\mu\text{m}$, given sufficient dust at a large enough radius. The low resolution of SST also made it difficult to separate stellar and diffuse emission. The velocities required were plausible. The problem was that expansion inexorably reduces the optical depth and so the veil either had to clear on ~ 10 year time scales or the mass and energy budget required to maintain it became unphysical. The disk geometry can reduce the mass and energy

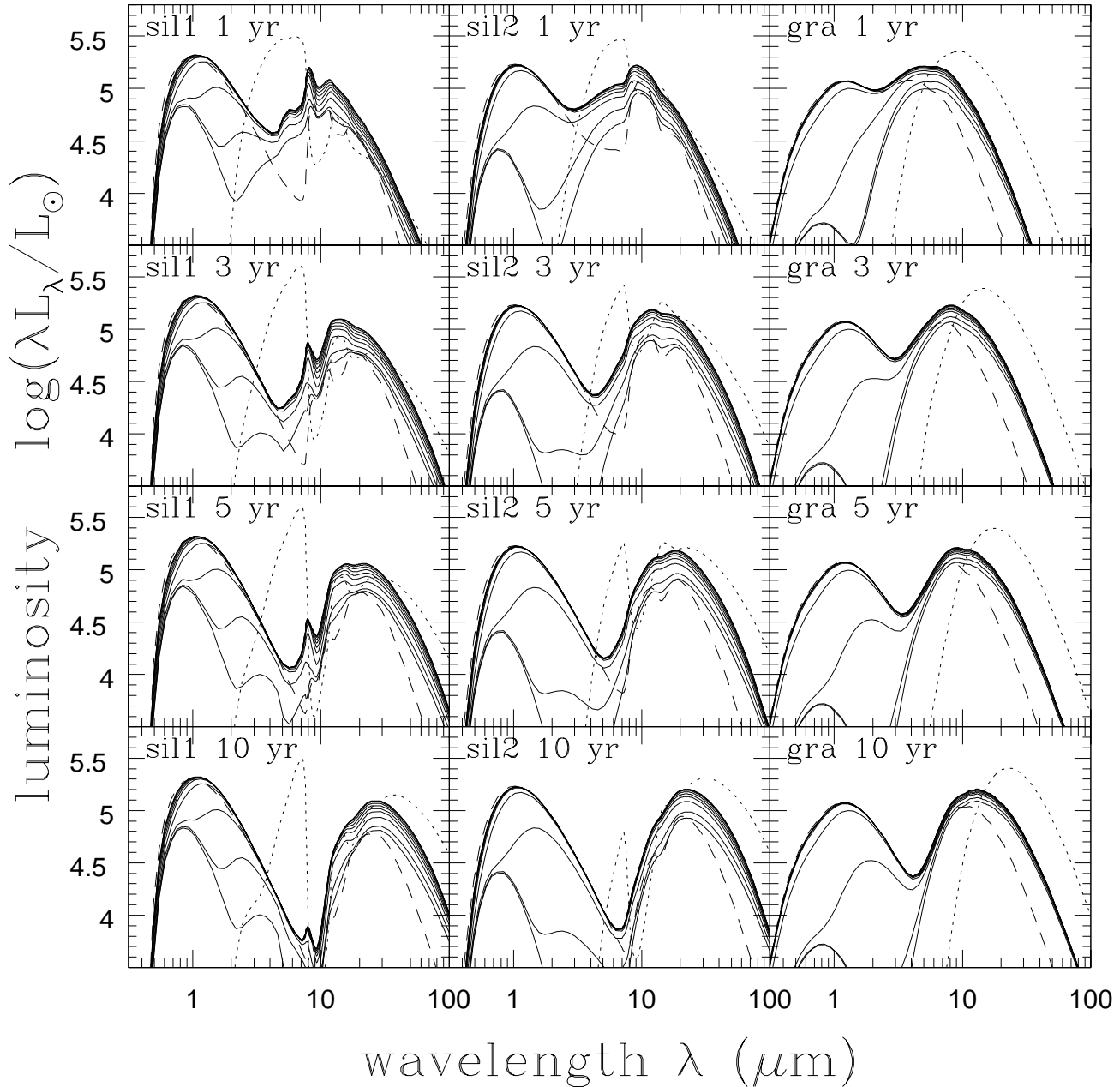


Figure 10. Inclination dependent SEDs as in Figs. 3-7 for $\eta = 8$ and fixed $\tau_e = 100$ and $\tau_p = 1$ as a function of time, with $\Delta t = 1$ year (top), 3, 5 and 10 years (bottom) for the sil1 (left), sil2 (middle) and gra (right) dusts. The SEDs are again shown for inclinations of 0° (pole-on) to 90° (edge-on) in increments of 10° and the dotted and dashed lines are for spherical models with optical depths of τ_e and τ_p , respectively. This is not a real time sequence since we are holding the optical depths fixed rather than dropping them as Δt^{-2} .

requirements to maintain the absorption at later times, but they must be quite geometrically thin to produce a large drop in either.

It is essentially impossible to hide survivors of relatively nearby transients like SN 1997bs, SN 2008S or NGC 6946-BH1 from JWST. With excellent point source sensitivity out to $25\mu\text{m}$, the mid-IR emission peak predicted in either the spherical or disk models is observable for decades. Putting the dust at a large enough distance to put the peak emis-

sion well beyond $25\mu\text{m}$ requires impossible masses, kinetic energies and elapsed times.

ACKNOWLEDGMENTS

CSK is supported by NSF grant AST-1908570.

DATA AVAILABILITY STATEMENT

All results can be replicated using the publicly available software package **RADMC-3D** (Dullemond et al. 2012).

REFERENCES

- Adams S. M., Kochanek C. S., 2015, *MNRAS*, 452, 2195.
doi:10.1093/mnras/stv1409
- Adams S. M., Kochanek C. S., Prieto J. L., Dai X., Shappee B. J., Stanek K. Z., 2016, *MNRAS*, 460, 1645.
doi:10.1093/mnras/stw1059
- Adams S. M., Kochanek C. S., Gerke J. R., Stanek K. Z., Dai X., 2017, *MNRAS*, 468, 4968.
doi:10.1093/mnras/stx816
- Andrews J. E., Jencson J. E., Van Dyk S. D., Smith N., Neustadt J. M. M., Sand D. J., Kreckel K., et al., 2021, *ApJ*, 917, 63. doi:10.3847/1538-4357/ac09e1
- Basinger C. M., Kochanek C. S., Adams S. M., Dai X., Stanek K. Z., 2021, *MNRAS*, 508, 1156.
doi:10.1093/mnras/stab2620
- Bear E., Soker N., Kashi A., 2022, *ApJ*, 934, 60.
doi:10.3847/1538-4357/ac7a9d
- Bond H. E., Henden A., Levay Z. G., Panagia N., Sparks W. B., Starrfield S., Wagner R. M., et al., 2003, *Natur*, 422, 405. doi:10.1038/nature01508
- Dominik C., Min M., Tazaki R., 2021, *ascl.soft*.ascl:2104.010
- Dorschner J., Begemann B., Henning T., Jaeger C., Mutschke H., 1995, *A&A*, 300, 503
- Draine B. T., 2003, *ApJ*, 598, 1017.
doi:10.1086/37911810.48550/arXiv.astro-ph/0304060
- Dullemond C. P., Juhasz A., Pohl A., Sereshti F., Shetty R., Peters T., Commercon B., et al., 2012, *ascl.soft*.ascl:1202.015
- Gerke J. R., Kochanek C. S., Stanek K. Z., 2015, *MNRAS*, 450, 3289. doi:10.1093/mnras/stv776
- Humphreys R. M., Davidson K., 1994, *PASP*, 106, 1025.
doi:10.1086/133478
- Ivezic, Z., & Elitzur, M. 1997, *MNRAS*, 287, 799
- Ivezic Z., Nenkova M., Elitzur M., 1999, *arXiv*, astro-ph/9910475. doi:10.48550/arXiv.astro-ph/9910475
- Kashi A., Soker N., 2017, *MNRAS*, 467, 3299.
doi:10.1093/mnras/stx240
- Kochanek C. S., 2011, *ApJ*, 741, 37. doi:10.1088/0004-637X/741/1/37
- Min M., Hovenier J. W., de Koter A., 2005, *A&A*, 432, 909.
doi:10.1051/0004-6361:2004192010.48550/arXiv.astro-ph/0503068
- Prieto J. L., Kistler M. D., Thompson T. A., Yüksel H., Kochanek C. S., Stanek K. Z., Beacom J. F., et al., 2008, *ApJL*, 681, L9. doi:10.1086/589922
- Thompson T. A., Prieto J. L., Stanek K. Z., Kistler M. D., Beacom J. F., Kochanek C. S., 2009, *ApJ*, 705, 1364.
doi:10.1088/0004-637X/705/2/1364
- Ueta T., Meixner M., 2003, *ApJ*, 586, 1338.
doi:10.1086/367818
- Van Dyk S. D., Peng C. Y., King J. Y., Filippenko A. V., Treffers R. R., Li W., Richmond M. W., 2000, *PASP*, 112, 1532. doi:10.1086/317727